

# Modeling Dense Urban Wireless Networks with 3D Stochastic Geometry

Alexandre Mouradian

*Laboratoire des Signaux et Systèmes (L2S, UMR8506), Univ. Paris  
Sud-CNRS-CentraleSupélec, Université Paris-Saclay F-91192 Gif-sur-Yvette  
alexandre.mouradian@u-psud.fr*

---

## Abstract

Over the past decade, many works on the modeling of wireless networks using stochastic geometry have been proposed. Results about probability of coverage, capacity or mean interference, have been provided for a wide variety of networks (cellular, ad hoc, cognitive, sensors, etc). These results notably allow to tune network protocol parameters. Nevertheless, in their vast majority, these works assume that the wireless network deployment is flat: nodes are placed on the Euclidean plane. However, this assumption is disproved in dense urban environments where many nodes are deployed in high buildings. In this paper, we derive the exact form of the probability of coverage for the cases where the interferers form a 3D Poisson Point Process (PPP) and an approximation for the 3D Modified Matern Process (MMP). We compare the 3D model with the 2D model and with simulation results. We comment the adequacy of each model depending on the parameters of the nodes (emission power, reception threshold, MAC protocol, etc.) and the height of the buildings in the simulations.

*Keywords:* Urban Wireless Networks, 3D, Stochastic Geometry, CSMA

---

## 1. Introduction

Stochastic geometry has been largely used to study and design wireless networks, because in such networks the interference, and thus the capacity, is highly dependent on the positions of the nodes [1, 2]. Stochastic geometry indeed allows to take into account the spatial component for the analysis of wireless systems performance at a very low computational cost (in several

cases closed form expressions are available [1]). Nevertheless, most of the works in the literature focus on networks deployed on the Euclidean plane. The motivation for this work comes from the intuition that for dense urban networks such as WiFi private networks, sensor networks, connected objects, deployed in dense urban areas, modeling the network with all the nodes lying on a plane (as is necessarily done with 2D models) will lead to an inaccurate representation of the interference suffered by a receiver. For instance, in Fig. 1, a screen capture of the map tool of Open Mobile Network [3] is provided. This tool offers approximate locations of WiFi and cellular access points on a map. The data gathering is done by crowd-sourcing with a mobile application. In Fig. 1, if we ignore obvious position errors, we observe that the WiFi access points are often located very close to one another, as they are presumably in the same building. In reality, they might in fact reside at different heights in different floors. An estimation of the interference suffered by a user based on this map would largely overestimate the real interference because the third dimension is not taken into account: the nodes are all projected on the same plane resulting in an unrealistic intensity of nodes.

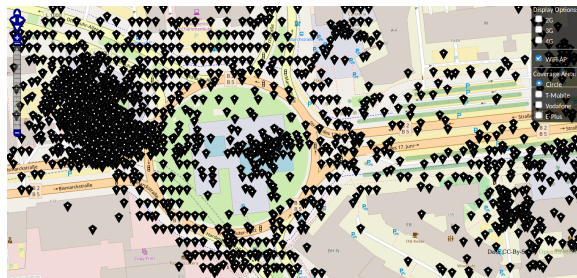


Figure 1: 2D map of the WiFi AP near TU Berlin retrieved on the 22nd of November 2017 at <http://map.openmobilenetwork.org/>

We think that with the explosion of the number of devices expected in the ISM bands, notably because of smartphones, tablets, connected objects (Internet of Things) and sensors, there is a need for an accurate modeling of the interference suffered by such devices in dense urban areas where the vertical component is not negligible. Indeed, accurate interference modeling is essential in order to design efficient mitigation mechanisms at different layers (medium access schemes, coding schemes, retransmission mechanisms, robust routing, etc.). In order to be accurate, the third space dimension has to be taken into account.

Throughout this paper, we model the node positions as a Poisson Point Process (PPP). We argue that the PPP seems to be a good model for dense urban areas where many networks are concurrently deployed in the same frequency bands (notably ISM bands) in a chaotic manner. Unlike cellular networks, for WiFi, sensor and IoT networks no planned deployment can be assumed in general [4].

For the numerical applications, we take the example of private WiFi networks in a dense urban area such as the center of Paris. We consider the *VIIe arrondissement* of Paris which contains around 32500 dwellings [5] and covers a surface of 2.15km<sup>2</sup>. We assume that each dwelling has one WiFi router. In the 2D model case, all the nodes have to lie on a plane and are distributed according to a Poisson Point Process (PPP). We can compute the intensity of the PPP in this case by dividing the number of routers by the area of the considered zone, yielding  $\lambda = 1.51 \times 10^{-2}$  nodes per  $m^2$ . In the 3D case, we can place the nodes in a volume, it means that we can take into account the building height. Therefore, the nodes are also spread on the  $z$  axis. If we assume a building height of 20 meters, dividing the number of routers by the volume of the considered area gives an intensity of  $\rho = 7.56 \times 10^{-4}$  nodes per  $m^3$ . We can notice that in this scenario  $\rho = \frac{\lambda}{20}$ . These intensities may seem high, but they actually do not take into account the devices (laptops and smartphones for instance) connected to the routers which also increase the interference.

The 3D model seems appealing for dense urban zone where the nodes are also distributed vertically. Nevertheless, the equations derived with stochastic geometry usually apply to an infinite space [1]. In the 2D case, this assumption seems reasonable since the studied networks usually cover a large surface compared to the range of the nodes, so it limits the impact of the border effects. In the 3D case, border effect may be more problematic because of the relatively small height of the building compared to the range of the devices. Therefore, in Section 4, we compare the numerical results obtained from the equations with simulation where the nodes are distributed in a limited zone along the  $z$  axis in order to investigate this aspect.

In the remainder of this paper, we derive the probability of coverage, first with no medium access control (the results are applicable to ALOHA [1]), and then with a CSMA access when nodes are distributed according to a 3D PPP.

The main contributions of this paper are as follows:

- we give an approximation of the probability of coverage for CSMA access in the 3D case;
- we compare 2D, 3D analytical models and simulation in order to determine the most suited model depending on the parameters of nodes and the network topology (notably the height of the deployment along the  $z$  axis).

The paper is organized as follows. Section 2 presents and comments related works on stochastic geometry and 3D network modeling. In Section 3.1, we derive the exact form of the probability of coverage for PPP interference for arbitrary emitter-receiver distance. It gives us insights on the problem for a simple case. In Section 3.2, we present the Modified Matern Process used to model CSMA access and derive an approximation of the probability of coverage for the 3D case. In section 4, we compare the numerical results obtained from the models of Section 3 with 2D models and simulation. Section 5 concludes the discussion and provides potential future developments.

## 2. Related works

Even if most of the research efforts are focused on 2D networks, 3D networks have been emerging during the past few years. It is notably the case for WSNs [6, 7, 8] underwater mobile networks [9] Unmanned Aerial Vehicle (UAV) networks [10]. From a more theoretical point of view, 3D networks have been investigated in terms of capacity [11, 12] and scaling laws have been provided. Nevertheless, in the present work we focus on the stochastic geometric approach to the study of wireless networks in the sense of [1, 2]. This approach has the advantage to provide tractable results for the probability of coverage in the case of the PPP model and good approximations for other models [1]. Whereas many theoretical works, focusing on stochastic geometry for wireless networks, consider dimension  $d$  [1, 2], when it comes to applications to specific cases, the chosen space is nearly always the Euclidean plane [13, 1, 14]. The only work explicitly covering the 3D case, to the best of our knowledge, is the recent [15]. In this work, the authors derive the probability of coverage with the two slopes propagation model for a 3D PPP. This work considers cellular networks, the receiver is thus attached to the nearest point of the PPP (the base station with the highest average received power). In our work, we first focus on a 3D PPP model as well, but with

a single slope propagation model and, more importantly, the receiver is receiving from an arbitrarily placed emitter. We argue that our model is more relevant in non operated ISM band networks such as WiFi, IoT, WSNs, etc, because the receiver cannot always connect to the closest node. Indeed, the closest node might not belong to the same network. Moreover, in our work, we mainly use the simple PPP model to easily compare simulation and theoretical models for different building heights (maximum value on the  $z$  axis) and thus evaluating the relevance of the 3D approach. Additionally, we then move to the Modified Matern Process which is a more realistic model for CSMA networks.

Many works modeling CSMA access through stochastic geometry have emerged in the literature these past ten years [13, 16, 14]. These works are based on a modified version of the Matern Point Process for which the points cannot live too close to each others. This allows to model the contention radius of CSMA as follows. The nodes of the network form a PPP on the Euclidean plane and they contend to access to the medium. Each node picks uniformly a value between zero and one, the node is selected in the process if it does not detect any node with a smaller mark value (this models the backoff procedure). The resulting process is the Modified Matern Process (MMP) which will be detailed in Section 3.2. As there is no known exact formulation of the interference in such process, [13, 16] and [14] use approximation techniques. They show that their approximations lie close to simulation results. We extend these works by considering 3D distribution of the nodes and compare the resulting model to simulation. To the best of our knowledge, this has not been considered in the literature.

In the remainder of this paper, we show how the probability of coverage is changed when going from 2D to 3D for Poisson distributed nodes in the simple case where all nodes can be interferers, and in the case a CSMA access protocol is used. We compare the theoretical prediction with simple simulations in order to investigate the impact of the border effect on the results. We also show that going from 2D to 3D is not trivial especially in the CSMA case because changing the dimension dramatically affects the form and thus the tractability of the expressions.

### 3. 3D models

In this part, we present two stochastic geometry models: 3D PPP and 3D MMP. We derive the closed form of probability of coverage for the former

and an approximation for the later.

### 3.1. 3D Poisson Point Process interference

In this section, we derive the probability of coverage for a terminal at distance  $d$  from the emitter when the interferers are distributed according to a PPP  $\Phi$  in  $\mathbb{R}^3$ . Whereas it is already given for  $\mathbb{R}^n$  and for  $\mathbb{R}^2$  in [1], here we find interesting to emphasize the differences between the 3D and 2D cases, and to show that considering the latter can lead to inaccurate representation of the interference. We consider an interference limited network. We thus use the Signal to Interference Ratio (SIR), which is defined as follows:

$$SIR = \frac{hd^{-\alpha}}{I}, \quad (1)$$

with  $h$  the fading coefficient between the emitter and receiver,  $d$  the emitter-receiver distance,  $\alpha$  the pathloss exponent and  $I = \sum_{x_i \in \Phi} g_i r_i^{-\alpha}$  the interference where  $g_i$  is the fading coefficient between the interferer  $x_i \in \Phi$  and the receiver and  $r_i$  the distance between them. As in [13, 17], we assume that all the nodes emit with the same power so it is simplified in the expression of the SIR. We have to note that unlike many works in the literature, we do not consider that the receiver is connected to the nearest node of the PPP because it is not always the case for the type of networks we consider (private WiFi is a good example) so the probability of coverage depends on the emitter-receiver distance. The probability of coverage is defined as the probability that the SIR is over a given threshold  $\beta$ :

$$P_c(\rho, \beta, \alpha, d) \equiv P\{SIR > \beta\}. \quad (2)$$

Its expression, when considering Rayleigh fading between the emitter and receiver, can be derived by the classic argument notably found in [1] and is equal to the Laplace transform of the interference shot noise in interference limited networks:

$$\begin{aligned} P_c(\rho, \beta, \alpha, d) &\stackrel{(a)}{=} \mathbb{E}_I[e^{-\mu d^\alpha \beta I}] \\ &= \mathcal{L}_I(\mu \beta d^\alpha), \end{aligned} \quad (3)$$

where (a) follows from  $H \sim \exp(\mu)$ .

We derive the expression of the Laplace transform for the 3D PPP case as follows:

$$\begin{aligned}
& \mathcal{L}_I(\mu\beta d^\alpha) \\
&= \mathbb{E}_{G_i, R_i} [e^{-\mu d^\alpha \beta \sum_{x_i \in \Phi} g_i r_i^{-\alpha}}] \\
&\stackrel{(b)}{=} \mathbb{E}_{R_i} [\prod_{x_i \in \Phi} \mathbb{E}_{G_i} [e^{-\mu d^\alpha \beta g_i r_i^{-\alpha}}]] \\
&\stackrel{(c)}{=} e^{-\rho \int_0^{+\infty} \int_0^{2\pi} \int_0^\pi (1 - \mathbb{E}_{G_i} [e^{-\mu d^\alpha \beta g_i r_i^{-\alpha}}]) r_i^2 \sin\theta_i dr_i d\theta_i d\phi_i} \\
&\stackrel{(d)}{=} e^{-\rho 4\pi \int_0^{+\infty} (1 - \frac{1}{1 + \beta d^\alpha r_i^{-\alpha}}) r_i^2 dr_i} \\
&\stackrel{(e)}{=} e^{-\rho 4\pi \frac{d^3}{3} \beta^{3/\alpha} \int_0^{+\infty} (\frac{1}{1+u^{\alpha/3}}) du}, \tag{4}
\end{aligned}$$

where (b) follows from  $G_i$  being i.i.d. and independence with  $R_i$ , (c) follows from the probability generating functional of the PPP [18], (d) follows from the MGF of  $G_i \sim \exp(\mu)$  and (e) with the change of variable  $u = \left(\frac{r_i}{d\beta^{1/\alpha}}\right)^3$ .

It differs from the 2D case which is given by  $e^{-\lambda\pi d^2 \beta^{2/\alpha} \int_0^{+\infty} (\frac{1}{1+v^{\alpha/2}}) dv}$ . We note that the solution of the integral in the general case (dimension  $D$ ) is:

$$\int_0^{+\infty} \left(\frac{1}{1+s^{\alpha/D}}\right) ds = s \times {}_2F_1\left(1, \frac{D}{\alpha}, \frac{D}{\alpha} + 1, -s^{\alpha/D}\right), \tag{5}$$

with  ${}_2F_1$  the Gaussian hypergeometric function. This function gives highly different values even for the same pathloss exponent  $\alpha$  in the 2D and the 3D cases. The other main difference is the exponential decay which is in  $d^2$  in the 2D case and  $d^3$  in 3D. We give the closed form for  $\alpha = 4$  for the 3D case:

$$P_c(\rho, \beta, 4, d) = e^{-\rho(4/2^{3/2})\pi^2 d^3 \beta^{3/4}}. \tag{6}$$

In the 2D case, it is:

$$P_c(\lambda, \beta, 4, d) = e^{-\lambda\pi^2 d^2 \beta^{1/2}/2}. \tag{7}$$

If we assume a slowly varying channel, we can define the average capacity in bits per seconds as a function of the probability of coverage [19] (Section 4.2.3 p.96):

$$C = P_c(\rho, SIR_{min}, 4, d) B \log_2(1 + SIR_{min}). \tag{8}$$

In this case, the transmitter encodes the data for a rate of  $B \log_2(1 + SIR_{min})$  and the data is correctly received if the  $SIR$  is greater or equal to  $SIR_{min}$ .  $B$  is the channel bandwidth in Hz. The capacity is given in bits per second.

In Section 4, we compare numerical results from the 2D and 3D PPP models. Furthermore, we compare the model predictions with simulation results when the space has a finite height (in order to model nodes placed in buildings).

In Section 3.2, we focus on the modeling of a more realistic setup: a 3D CSMA network. Nevertheless, we can note that expression (6) is valid for modeling an ALOHA medium access. In this case, the intensity of the process should be multiplied by the probability for a node to emit [1]. ALOHA access is currently one of the considered access mechanisms in the IoT standard LoRaWAN [20] from the LoRa Alliance [21]. The 3D PPP model could thus be used to model such IoT networks in dense urban areas.

In the next part of this paper, we consider another medium access model: CSMA. More precisely, we extend to  $\mathbb{R}^3$  an approximation of the probability of coverage for the MMP model. We then compare the theoretical model predictions to simulation results in Section 4.

### 3.2. 3D Modified Matern Process interference

In this section, we treat the 3D case for the Modified Matern type II Process (MMP) which is considered in many works [13, 14] in order to model CSMA access. With this model, nodes too close to each others cannot transmit at the same time, interference is thus reduced. The MMP model is detailed in Section 3.2.1.

Since the exact Laplace functional is not known for the MMP, the technique used in the previous section for PPP (notably step (c) in equation (4)) cannot be applied directly. In previous works, several different approximation techniques are used [13, 17, 16, 14]. In this paper, we use the technique which consists in:

1. assuming a finite region containing the potential contenders for a node;
2. deriving the resulting MMP intensity  $\rho_{csma}$ ;
3. considering only dominant interferers;
4. approximating the MMP with a PPP of intensity  $\rho_{csma}$  outside of the emitter contention domain.

This approximation technique is notably used in [14] for an alternative version of the MMP. In our work, we derive expressions for the 3D case,

whereas [14] is only for the 2D case and the alternative MMP. The main differences from the literature come from: the use of Rayleigh fading in Equations (9) (11) (14) (16) and (18) and the impact of 3D in Equations (11) (16) and (18). Concerning the remaining equations, the impact of going from 2D to 3D is small on the derivations (notably for Equations (10) and (15) whose derivation are given in Appendix A and Appendix B for the sake of completeness). The presented approximation technique allows to obtain an expression of the probability of coverage for the MMP, despite the fact that the exact expression is not known. It is detailed for the 3D case in the remainder of this section.

### 3.2.1. The Modified Matern type II Process

In this part of the paper, we use a modified version of the Matern type II process [13]. The classic Matern type II process is built from a marked PPP: each point of the PPP is marked with a real number  $m \in [0, 1]$  and the PPP is thinned by retaining only the points which have the smallest mark in a ball of radius  $D$  centered on themselves. Formally,  $\Phi_m = \{x_i \in \Phi | m_i < m_j, \forall x_j \in \Phi \cap \mathcal{B}(x_i, D) \setminus x_i\}$ , with  $\Phi$  the PPP in  $\mathbb{R}^3$ ,  $m_i$  the mark of point  $x_i$  and  $\mathcal{B}(x_i, D)$  a ball of radius  $D$  centered on  $x_i$ . In the modified version of the process, there is no fixed radius  $D$ , but the radius is replaced by the notion of detection: a node from the marked PPP is kept in the MMP if it does not detect any signal from a node with a lower mark. The signal from a node is detected if it is above a threshold  $T_d$ . So formally the process is defined as  $\Phi_m = \{x_i \in \Phi | m_i < m_j, \forall x_j : P_t h_{ij} r_{ij}^{-\alpha} \geq T_d\}$ , with  $P_t$  the transmission power,  $h_{ij}$  and  $r_{ij}$  the fading coefficient and distance between  $x_i$  and  $x_j$  respectively.

The MMP allows to model the position of the nodes accessing the medium concurrently with a CSMA MAC scheme. The underlying PPP represents the positions of the nodes. In the following subsections, we detail the steps of the aforementioned approximation technique applied to the 3D case.

### 3.2.2. Defining a finite region for contenders

In reality, the region which contains the contenders of a given node (the nodes which can be detected by that node) presents an irregular shape because of the randomness of the fading coefficients. Nevertheless, as mentioned previously, the first step of the approximation technique consists in considering a fixed radius, called the detection radius (denoted  $r_d$ ), outside of which the probability (denoted  $\epsilon_d$ ) that a node is detected is arbitrary low. Thus

the contenders of a node  $x_i$  are contained in  $\mathcal{B}(x_i, r_d)$  which is a ball in the 3D case. It allows to simplify the expressions without losing too much accuracy [14]. Formally, the detection radius is defined as follows:

$$\begin{aligned} P(P_t h_{ij} r_d^{-\alpha} \geq T_d) \leq \epsilon_d &\Leftrightarrow r_d = \left( \frac{P_t}{T_d} F_{H_{ij}}^{-1}(\epsilon_d) \right)^{1/\alpha} \\ &\Leftrightarrow r_d = \left( \frac{P_t - \ln(\epsilon_d)}{T_d \mu} \right)^{1/\alpha}, \end{aligned} \quad (9)$$

if we consider  $H_{ij} \sim \exp(\mu)$ .

### 3.2.3. The intensity of the Modified Matern Process

The intensity of the resulting process (considering only contenders in  $\mathcal{B}(x_i, r_d)$ ) is given as  $\rho_{csma} = \rho P_{csma}$  [18], with  $P_{csma}$  the probability for a node of the underlying PPP to be retained and  $\rho$  the intensity of the PPP. Thus  $P_{csma}$  is the probability that among the contenders of a node  $x_i$  (the nodes of  $\Phi$  which are inside  $\mathcal{B}(x_i, r_d)$  and that are detected by  $x_i$ ) none have a smaller mark than  $x_i$ .

Formally, it is given as:

$$\begin{aligned} P_{csma} &= \sum_{k=0}^{+\infty} \sum_{n=k}^{+\infty} \frac{1}{1+k} P_n \binom{n}{k} P_d^k (1 - P_d)^{n-k} \\ &= \frac{1 - e^{-\rho(4/3)\pi r_d^3 P_d}}{\rho(4/3)\pi r_d^3 P_d}. \end{aligned} \quad (10)$$

The details of the argument can be found in Appendix A (it is given for the sake of completeness since it is similar to arguments in [13] or [14]).  $P_n$  and  $P_d$  are respectively the probability to have  $n$  nodes in  $\mathcal{B}(x_i, r_d)$  and the probability to detect a node which is in  $\mathcal{B}(x_i, r_d)$ .  $P_n$  is thus the probability that there are  $n$  nodes in a volume of  $(4/3)\pi r_d^3$  which is given by the Poisson

distribution. Concerning  $P_d$ , in the 3D case we have:

$$\begin{aligned}
P_d &= P(P_t h_{ij} r_{ij}^{-\alpha} \geq T_d) \\
&= \mathbb{E}_{R_{ij}} \left[ e^{-\mu T_d r_{ij}^\alpha / P_t} \right] \\
&\stackrel{(f)}{=} \int_0^{r_d} \frac{3r_{ij}^2}{r_d^3} e^{-\mu T_d r_{ij}^\alpha / P_t} dr_{ij} \\
&= \frac{3}{r_d^3} \frac{\Gamma(\frac{3}{\alpha}) - \Gamma(\frac{3}{\alpha}, \frac{\mu T_d r_d^\alpha}{P_t})}{\alpha \left(\frac{\mu T_d}{P_t}\right)^{3/\alpha}}, \tag{11}
\end{aligned}$$

with  $\Gamma(a)$  and  $\Gamma(a, b)$  the Gamma function and incomplete upper Gamma function, (f) follows from  $H_{ij} \sim \exp(\mu)$ , and:

$$f_{R_{ij}}(r_{ij}) = \frac{3r_{ij}^2}{r_d^3}, \tag{12}$$

is the density function of the random distance between  $x_i$  and  $x_j$  in  $\mathcal{B}(x_i, r_d)$ . In order to prove that expression (12) is correct for the 3D case (for the 2D case it is given in [22]) we have to remember that  $x_j$  is uniformly placed in  $\mathcal{B}(x_i, r_d)$  because of the underlying PPP properties, so we have  $F_{R_{ij}}(r_{ij}) = \frac{(4/3)\pi r_{ij}^3}{(4/3)\pi r_d^3}$ . Taking the derivative with respect to  $r_{ij}$  yields the result. Expression (11) differs from the 2D case where  $f_{R_{ij}}(r_{ij})$  is  $\frac{2r_{ij}}{r_d^2}$  [22], but the expression remains reasonably easy to compute in the 3D case (the Gamma functions can be efficiently computed).

From (10) and  $\rho_{csma} = \rho P_{csma}$ , we conclude that the intensity of the MMP is:

$$\rho_{csma} = \frac{1 - e^{-\rho(4/3)\pi r_d^3 P_d}}{(4/3)\pi r_d^3 P_d}. \tag{13}$$

#### 3.2.4. Dominant interferers vulnerability radius

Once we have obtained the intensity of the MMP, we consider only the interferers which can corrupt the signal on their own, and we assume that they all lie in a region around the receiver, called the vulnerability region. Similarly to the detection radius, we define the vulnerability radius as the radius for which nodes beyond that limit have an arbitrary low probability

(noted  $\epsilon_v$ ) to make the SIR at the receiver drop under the reception threshold. The receiver is placed at the origin and noted  $o$ . The emitter is part of the process and noted  $x_i$ . Formally the vulnerability radius is defined as follows:

$$\begin{aligned}
P\left(\frac{h_{io}r_{io}^{-\alpha}}{h_{jo}r_v^{-\alpha}} \leq \beta\right) \leq \epsilon_v &\Leftrightarrow \epsilon_v = F_{\frac{H_{io}}{H_{jo}}}\left(\beta\frac{r_v^{-\alpha}}{r_{io}^{-\alpha}}\right) \\
&\Leftrightarrow r_v = r_{io}\left(\beta\frac{1-\epsilon_v}{\epsilon_v}\right)^{1/\alpha}, \tag{14}
\end{aligned}$$

with  $\frac{H_{io}}{H_{jo}}$  the ratio of exponential random variables of parameter  $\mu$  so  $F_{\frac{H_{io}}{H_{jo}}}(l) = 1 - \frac{1}{1+l}$ .

### 3.2.5. Probability of coverage

We give an approximation of the probability of coverage ( $P_c^{csma}$ ) for a typical receiver at the origin. As previously mentioned, the MMP is approximated with a PPP of the same intensity outside of the contention domain of the emitter  $x_i$ , this approximation is known to be very close to simulation results [23]. In this context, the probability of outage is the probability that among the nodes in the vulnerability radius which coexist with  $x_i$  (outside of the contention region of  $x_i$ ) some will be able to make the SIR drop under the threshold  $\beta$ . The probability of coverage is the complement of the probability of outage:

$$\begin{aligned}
P_c^{csma} &= 1 - \sum_{k=1}^{+\infty} \sum_{n=k}^{+\infty} \sum_{l=1}^k P_n \binom{n}{k} (1 - P_{d'})^k P_{d'}^{n-k} \binom{k}{l} P_\beta^l (1 - P_\beta)^{k-l} \\
&= e^{-K_{csma} P_\beta (1 - P_{d'})}, \tag{15}
\end{aligned}$$

with  $P_n = \frac{(K_{csma})^n e^{-K_{csma}}}{n!}$ ,  $K_{csma} = \rho_{csma} (4/3) \pi r_v^3$ ,  $P_{d'}$  and  $P_\beta$  are respectively the probability that a node coexists with the emitter and the probability that the SIR drops under the reception threshold.  $P_{d'}$  and  $P_\beta$  are derived below in this section. The full detail argument for Equation (15) can be found in Appendix B. Again, the derivation is similar to the 2D case in [14]. Nevertheless, deep differences from the 2D case are found in the expressions of  $P_{d'}$  and  $P_\beta$  derived below (and also in expression (13) of  $\rho_{csma}$  as shown in Section 3.2.3).

$P_{d'}$  is the probability for a node in  $\mathcal{B}(o, r_v)$  to be in the contention domain of  $x_i$  (to be detected by  $x_i$ ):

$$\begin{aligned}
P_{d'} &= P(P_t h_{ij} r_{ij}^{-\alpha} \geq T_d) \\
&= \mathbb{E}_{R_{ij}} \left[ P \left( h_{ij} \geq \frac{T_d r_{ij}^\alpha}{P_t} \middle| r_{ij} \right) \right] \\
&= \int_0^{r_v+r_{io}} f_{R_{ij}}(r_{ij}) e^{-\mu T_d r_{ij}^\alpha / P_t} dr_{ij} \\
&= \frac{3\Gamma\left(\frac{3}{\alpha}\right) - 3\Gamma\left(\frac{3}{\alpha}, A\right)}{\alpha r_v^3 \left(\frac{\mu T_d}{P_t}\right)^{\frac{3}{\alpha}}} \\
&\quad + \left[ 3C(-r_v^4 - 2r_{io}r_v^3 + 2r_{io}^3r_v + r_{io}^4) A^{(4/\alpha)} B^{(2/\alpha)} \right. \\
&\quad - 6D(r_{io}r_v^3 + 3r_{io}^2r_v^2 + 3r_{io}^3r_v + r_{io}^4) A^{(4/\alpha)} B^{(1/\alpha)} \\
&\quad + 3E(r_v^4 + 4r_{io}r_v^3 + 6r_{io}^2r_v^2 + 4r_{io}^3r_v + r_{io}^4) A^{(4/\alpha)} \\
&\quad + B^{(4/\alpha)} \left\{ 3F(r_v^4 - 2r_{io}r_v^3 + 2r_{io}^3r_v - r_{io}^4) A^{(2/\alpha)} \right. \\
&\quad + 6G(r_{io}r_v^3 - 3r_{io}^2r_v^2 + 3r_{io}^3r_v - r_{io}^4) A^{(1/\alpha)} \\
&\quad \left. \left. + 3H(-r_v^4 + 4r_{io}r_v^3 - 6r_{io}^2r_v^2 + 4r_{io}^3r_v - r_{io}^4) \right\} \right] \\
&\quad / \left[ 4\alpha r_{io}r_v^3 A^{(4/\alpha)} B^{(4/\alpha)} \right], \tag{16}
\end{aligned}$$

with  $A = \left(\frac{\mu(r_v-r_{io})^\alpha T_d}{P_t}\right)$ ,  $B = \left(\frac{\mu(r_v+r_{io})^\alpha T_d}{P_t}\right)$ ,  $C = \Gamma(2/\alpha, B)$ ,  $D = \Gamma(3/\alpha, B)$ ,  $E = \Gamma(4/\alpha, B)$ ,  $F = \Gamma(2/\alpha, A)$ ,  $G = \Gamma(3/\alpha, A)$ , and  $H = \Gamma(4/\alpha, A)$ .

Here the expression of  $f_{R_{ij}}(r_{ij})$  changes from (12) in Section 3.2.3, because we are no more interested in  $\mathcal{B}(x_i, r_d)$  but rather in  $\mathcal{B}(o, r_v)$ . As can be seen in Fig. 2 we now have two cases: either  $\mathcal{B}(x_i, r_{ij})$ , the dotted sphere, is contained in  $\mathcal{B}(o, r_v)$ , the dashed sphere ( $0 \leq r_{ij} \leq r_v - r_{io}$ ), or it is not ( $r_v - r_{io} < r_{ij} \leq r_v + r_{io}$ ). In the first case, the expression is similar to (12). In the second case, the expression for  $f_{R_{ij}}(r_{ij})$  changes because we know that  $x_j$  cannot be outside of  $\mathcal{B}(o, r_v)$  so it must lie in the intersection of  $\mathcal{B}(x_i, r_{ij})$  and  $\mathcal{B}(o, r_v)$ :

$$f_{R_{ij}}(r_{ij}) \begin{cases} \frac{3r_{ij}^2}{r_v^3}, & \text{for } 0 \leq r_{ij} \leq r_v - r_{io}, \\ \frac{3r_{ij}(r_v-r_{io}+r_{ij})(r_v+r_{io}-r_{ij})}{4r_{io}r_v^3}, & \text{for } r_v - r_{io} < r_{ij} \leq r_v + r_{io}. \end{cases} \tag{17}$$

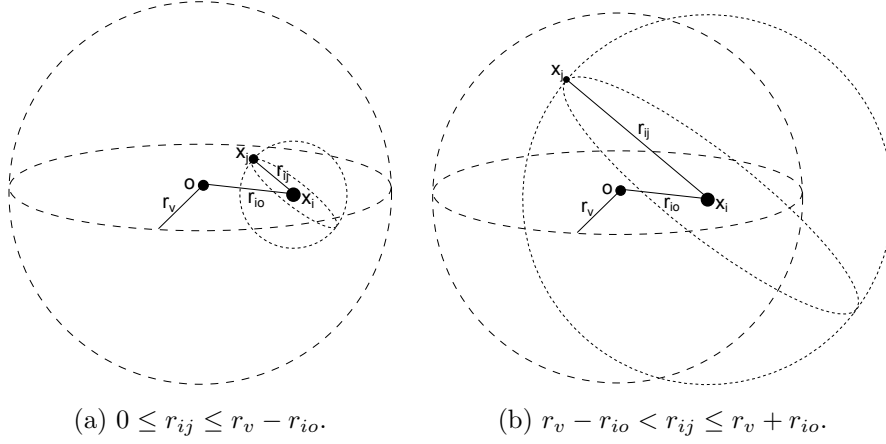


Figure 2: Representation of the distances  $r_{ij}$  and  $r_{io}$  in the vulnerability radius

Interestingly, we note that the second piece of the expression of  $f_{R_{ij}}(r_{ij})$  is rational whereas in the 2D case it includes trigonometric functions (see Appendix C). It allows to have an exact expression for  $P_{d'}$  in the 3D case (expression (16)) whereas, to the best of our knowledge, numerical integration has to be used in the 2D case (see Appendix C).

$P_\beta$  is the probability that a node in  $\mathcal{B}(o, r_v)$  is able to make the SIR at the receiver drop under the reception threshold  $\beta$ :

$$\begin{aligned}
P_\beta &= P\left(\frac{h_{io}r_{io}^{-\alpha}}{h_{jo}r_{jo}^{-\alpha}} \leq \beta\right) \\
&= \mathbb{E}_{R_{jo}}\left[P\left(\frac{h_{io}}{h_{jo}} \leq \beta r_{jo}^{-\alpha} r_{io}^\alpha\right)\right] \\
&= \int_0^{r_v} \frac{3r_{jo}^2}{r_v^3} F_{\frac{H_{io}}{H_{jo}}}(\beta r_{jo}^{-\alpha} r_{io}^\alpha) dr_{jo} \\
&\stackrel{(g)}{=} \int_0^{r_v} \frac{3r_{jo}^2}{r_v^3} \left(\frac{\beta}{\beta + \left(\frac{r_{jo}}{r_{io}}\right)^\alpha}\right) dr_{jo} \\
&\stackrel{(h)}{=} \frac{r_{io}^3}{r_v^3} \beta^{3/\alpha} \int_0^{\left(\frac{r_v}{r_{io}\beta^{1/\alpha}}\right)^3} \frac{1}{1+w^{\alpha/3}} dw \\
&= {}_2F_1\left(1, \frac{3}{\alpha}, \frac{3}{\alpha} + 1, -\left(\frac{r_v}{r_{io}\beta^{1/\alpha}}\right)^\alpha\right), \tag{18}
\end{aligned}$$

where  ${}_2F_1$  is the Gaussian hyper-geometric function, (g) follows from  $F_{\frac{H_{io}}{H_{jo}}}(l) = 1 - \frac{1}{1+l}$  and  $f_{R_{jo}}(r_{jo}) = \frac{3r_{jo}^2}{r_v^3}$ , and (h) from the change of variable  $w = \left(\frac{r_{jo}}{r_{io}\beta^{1/\alpha}}\right)^3$ .

In the CSMA case, with Equation (15), we have computed the probability of coverage when the emitter is part of the MMP. Therefore, in order to compute the capacity we have to modify Equation (8) to take into account that the node has to be selected before it can transmit:

$$C_{CSMA} = P_{CSMA} P_c^{CSMA} B \log_2(1 + SIR_{min}). \tag{19}$$

The terms are the same as Equation (8) with  $P_c^{CSMA}$  defined by Equation (15), and  $P_{CSMA}$  (Equation (10)) is the probability that a node of the underlying PPP is selected in the MMP. It thus takes into account the fact that the sender node has to be selected in the MMP in order to transmit.

## 4. Numerical and simulation results

In this section, we present numerical results obtained from the models described in Section 3. As stated in Section 1, the goal of this section is to compare the 2D and 3D PPP and MMP models with simulation results when a maximal building height is taken into account. This allows to investigate the impact of the border effect on the results given by the 3D model.

### 4.1. 3D Poisson Point Process

#### 4.1.1. Numerical results

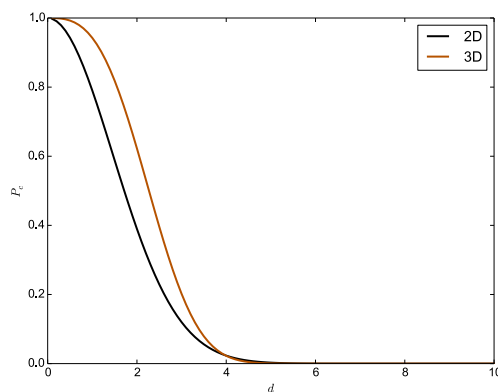


Figure 3: Probability of coverage as a function of the emitter-receiver distance for 2D and 3D PPP interference

In Fig. 3, we plot  $P_c(\rho, \beta, 4, d)$  for the 2D and 3D cases with  $\lambda = 1.51 \times 10^{-2}$  and  $\rho = 7.56 \times 10^{-4}$  (as motivated in Section 1),  $\mu = 1$ ,  $P_t = 100\text{mW}$ ,  $T_d = -76\text{dBm}$ ,  $\alpha = 4$  and  $\beta = 10$ , the plot is as a function of the emitter-receiver distance  $d$ . We observe that  $P_c$ , in the 2D case, is highly underestimated when the receiver is close to the emitter. Given the steepness of the decay, the error might be important: for instance, there is 0.23 absolute difference at 2 meters. We note that the  $P_c$  is getting very rapidly low (after few meters  $P_c$  goes to zero) which is not realistic. We observe this because, in this simple case, all the nodes transmit at the same time, whereas it is not the case in reality where a MAC protocol is used. Nevertheless, the results show important differences between 2D and 3D models. Results for the more realistic MMP model are proposed in Section 4.2.

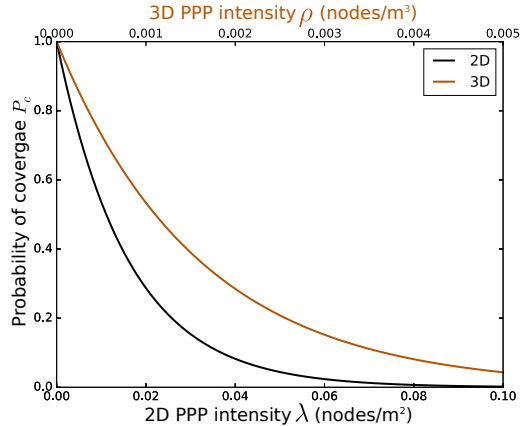


Figure 4: Probability of coverage as a function of the node intensity for 2D and 3D PPP interference

In Fig. 4, we compare the probability of coverage as a function of the intensity for  $d = 2m$ . As mentioned in Section 1, if we assume that the average building height is 20m, we have  $\rho = \frac{\lambda}{20}$ . This is because in the 2D case, all the nodes have no choice but to lie on the plane whereas in the 3D case they are also spread in the third dimension. In Fig. 4, we thus have two curves with different  $x$  axis scales in order to take into account this fact. We observe that both curves have an exponential decay with the 3D curve being over the 2D. Equation (8) defines the capacity of the channel under PPP interference as a function of the probability of coverage. Fig. 5 is a plot of the capacity for  $B = 20\text{MHz}$  and  $SIR_{min} = \beta$  ( $d$  is kept equal to 2m). The capacity is a product between the probability of coverage and a term depending on the bandwidth and the minimum SIR, so we observe in Fig. 5 the same type of exponential decay as in Fig. 4.

#### 4.1.2. Comparison with simulation results

In this section, we compare the theoretical and simulation results. We evaluate the relevancy of the 3D approach for dense urban areas by considering the following question: for which building height does it make sense to model the interference process as a 3D PPP? Indeed, in reality, the nodes will be spread within a finite height because of the limited height of the buildings, so a border effect may appear compared to the theoretical model.

The simulation setup is as follows: the point process is generated in a box of  $200m \times 200m \times Z$  with  $Z \in 10m, 50m, 100m$ . The 3D intensity of the

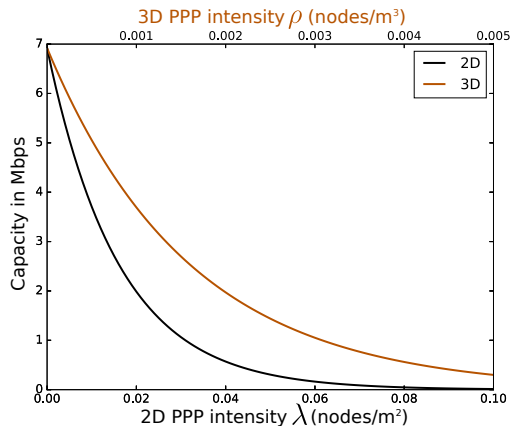


Figure 5: Capacity as a function of the node intensity for 2D and 3D PPP interference

process is calculated based on the 2D intensity:  $\rho = \frac{\lambda}{Z}$ . The reason for this is that in the 2D all the points have to lie on a plane, the intensity is thus maximal. In the 3D case, the points are also spread along the  $z$  axis. Then for each realization of the PPP, the SIR is computed at the origin (the center of the aforementioned box) thanks to equation (1). The simulation and model parameters are the following:  $\lambda = 1.51 \times 10^{-2}$  (we keep the values from the example of Section 1),  $\beta = 10$  and  $\alpha = 4$ . The emitter-receiver distance  $d$  varies from 0 to 10 meters. For the PPP case, the actual placement of the emitter does not matter, we only need to have the received signal strength computed with the emission power and random attenuation (numerator of Equation 1). Intuitively, this is because the emitter does not influence the interference as in the MMP case.

Fig. 6 depicts the comparison of the probability of coverage  $P_c$  between simulation and theoretical results for different building heights (parameter  $Z$ ) as a function of the emitter-receiver distance. For each simulation point,  $10^4$  PPP realizations are produced. The 95% confidence interval is plotted, but is barely visible (it is very small). The 2D model corresponds to the solid curve, we observe that it underestimates the probability of coverage compared to 3D models and simulations. The three dashed and dotted curves correspond to the 3D theoretical models. They are obtained from expression (6) with  $\rho = \frac{\lambda}{Z}$  and  $Z \in 10m, 50m, 100m$ . We observe, as expected, that the probability of coverage is higher when the considered height  $Z$  is greater because the nodes are more spread, and thus the distances to the interferers

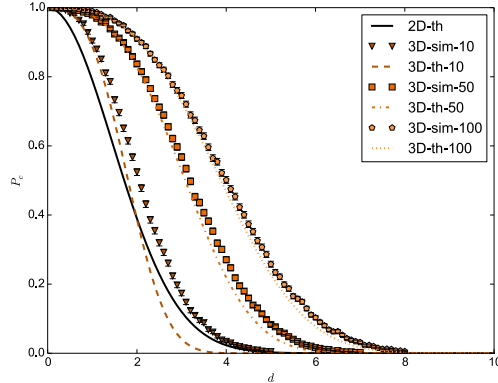


Figure 6: Comparison of theoretical and simulation results for PPP interference

are larger on average. For  $Z = 50\text{m}$  and  $Z = 100\text{m}$  the simulation matches the theoretical prediction very well. Nevertheless, a tiny deviation can be noticed at the tail of the curves. This deviation is larger for  $Z = 50\text{m}$  than for  $Z = 100\text{m}$ . In the  $Z = 10\text{m}$  case, the deviation of the theoretical model from the simulations is very significant. We can interpret these deviations as a border effect when the height of the box is reduced: the 3D theoretical model assumes no limits on the  $x$ ,  $y$  and  $z$  axis. We also observe that even when the height of the box is reduced to  $Z = 10\text{m}$  the 2D theoretical model is not a good representation of the simulation data either. In this case, we note that the 3D model is a better match for the start of the curve and the 2D model is better for the tail of the curve.

We conclude that the 3D model seems to be accurate enough when the box height is sufficiently large to avoid border effect. Moreover, even when the height is small (the  $Z = 10\text{m}$  case) 3D model still provides a good representation of the probability of coverage close to the emitter because the border effect is larger for longer emitter-receiver distances.

#### 4.2. 3D Modified Matern Process

In this part, we present the results for the MMP model.

##### 4.2.1. Numerical results

Fig. 7 depicts the probability of coverage for the 2D and 3D cases for the MMP.  $P_c^{csma}$  (Equation (15)) is given as a function of  $r_{io}$ , the emitter-receiver distance. The curves are plotted with the values  $P_t = 100\text{mW}$ ,

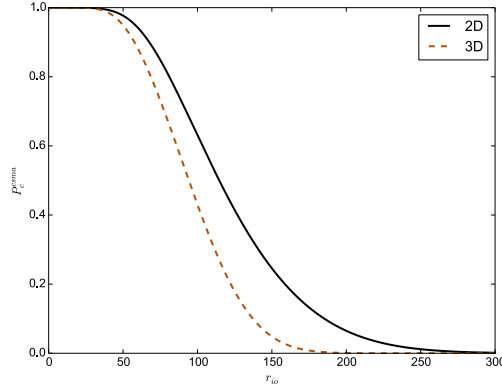


Figure 7: Probability of coverage for 2D and 3D MMP

$T_d = -76\text{dBm}$ ,  $\beta = 10$ ,  $\alpha = 4$ ,  $\mu = 1$ ,  $\epsilon_d = 10^{-6}$ ,  $\epsilon_v = 10^{-2}$ , and  $\rho$  and  $\lambda$  from Section 1. First we have to note that in this case, the communication range is more realistic (even if in reality in dense urban environments, we may encounter pathloss exponents greater than 4). We observe that, with the aforementioned parameter values, the probability of coverage is strictly higher in the 2D case for emitter-receiver distances greater than  $50\text{m}$ . We can interpret this result as follows: for the PPP in Section 3.1, we remarked that the 3D probability of coverage tends to drop later than the 2D, but then the slope is steeper. For the MMP model, the difference in the drop position is suppressed by the contention mechanism (it avoids close interferers), but the difference in the slopes remains.

As described in Section 3.2.3, the intensity  $\rho_{csm}$  of the point process representing the transmitters (the MMP) is different from the underlying PPP intensity  $\rho$ . Fig. 8 depicts the value of  $\rho_{csm}$  as a function of  $\rho$  (it corresponds to equation (13)), we observe that the value of  $\rho_{csm}$  converges toward a maximum value:  $\lim_{\rho \rightarrow \infty} \rho_{csm} = \frac{1}{(4/3)\pi r_d^3 P_d}$ . It means that, when the intensity of nodes increases, the intensity of interferers converges. In the remainder of the paper, we call this situation saturated condition. The convergence implies that even in the 2D case where all the nodes lie on the Euclidean plane, the intensity of interferers will not grow as much as in the PPP case. This implies that the probability of coverage as defined in Equation (15) does not varies as a function of the intensity when we are in saturated condition. Intuitively, this can be understood because of the

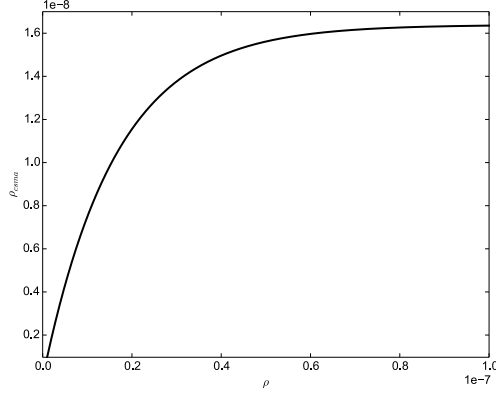


Figure 8: Intensity of the MMP as a function of the intensity of the underlying PPP

guard distance induced by the CSMA mechanism around the emitter which prevents close interferers even when the network is dense.

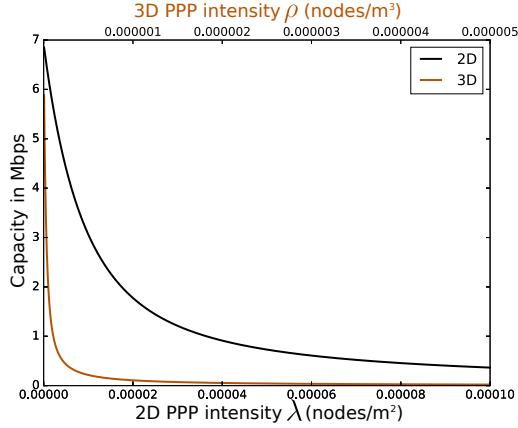


Figure 9: Capacity as a function of the underlying 2D and 3D PPP intensity for CSMA

Fig. 9 is a plot of the capacity as a function of the intensity of the process. Equation (19) is used with  $SIR_{min} = \beta$  and  $B = 20\text{MHz}$ ,  $P_c^{CSMA}$  is computed at 50m from the emitter. We use the same relation between  $\lambda$  and  $\rho$  as in Figs. 4 and 5 (20m building height). In this case, we observe that the capacity in 3D drops more rapidly than 2D when the number of nodes per measure unit increases. This is coherent with the interpretation of Fig. 7.

#### 4.2.2. Comparison with simulation results

In this section, we compare the 3D theoretical model with the 2D theoretical model and with simulation results. The goal, as in Section 4.1.2, is to evaluate the adequacy of 2D and 3D models to represent the probability of coverage for different node parameters and building heights. In this section, we experiment with two simulation setups: the first with 802.11 node parameters, and the second with node parameters representing 802.15.4 radios.

The first simulation setup is as follows: the underlying PPP is generated in a box of  $2000m \times 2000m \times Z$  with  $Z \in \{20m, 200m, 2000m\}$ . We use a larger box than for the PPP case, because otherwise we do not have enough nodes in the MMP after the thinning of the PPP through the contention process. The contention process consists in nodes picking a random mark uniformly in  $[0, 1]$ . Then each node checks if it can detect neighbors with a lower mark. A node is detected if the signal received is above a threshold (the signal strength depends on the transmission power, the distance, and on a fading random variable). If no detectable neighbor has a lower mark, the node is kept in the MMP.

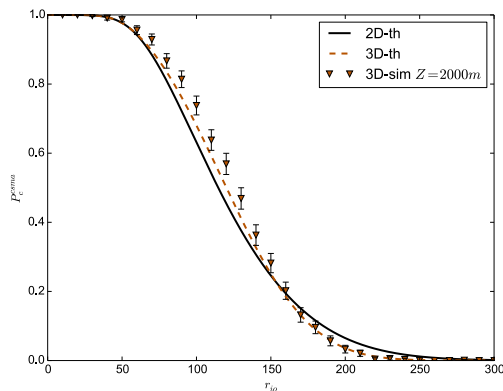


Figure 10: Comparison of theoretical and simulation results for the MMP model for  $Z = 2000m$

As in Section 4.1.2, the 3D intensity of the process is calculated based on the 2D intensity:  $\rho = \frac{\lambda}{Z}$ . In this case, we take  $\lambda = 7 \times 10^{-5}$  so that we have enough nodes in the box and the thinning process is not too long (it is notably very long for the parameters considered in Section 1). We will see that this value is important only if we are not in saturated condition (see

the comment on Fig. 8 in the previous section). For each realization of the MMP, we select the closest node to the center of the box to be the emitter, we then compute the SIR at  $r_{io}$  meters from the emitter (in direction of the center of the box) and check if it is over or below the reception threshold. We repeat this process  $10^3$  times for every  $r_{io}$ . The parameters of the node and the channel are as follows:  $P_t = 100\text{mW}$ ,  $T_d = -76\text{dBm}$ ,  $\beta = 10$ ,  $\alpha = 4$ , and  $\mu = 1$ .

Fig. 10 depicts the simulation results with  $Z = 2000\text{m}$  and 2D (solid curve) and 3D (dashed curved) model predictions for the probability of coverage. In this case, the 3D model is not in saturated condition. We observe that the 2D and 3D models yield very close values. Nevertheless, the simulation results closely follow the 3D model predictions.

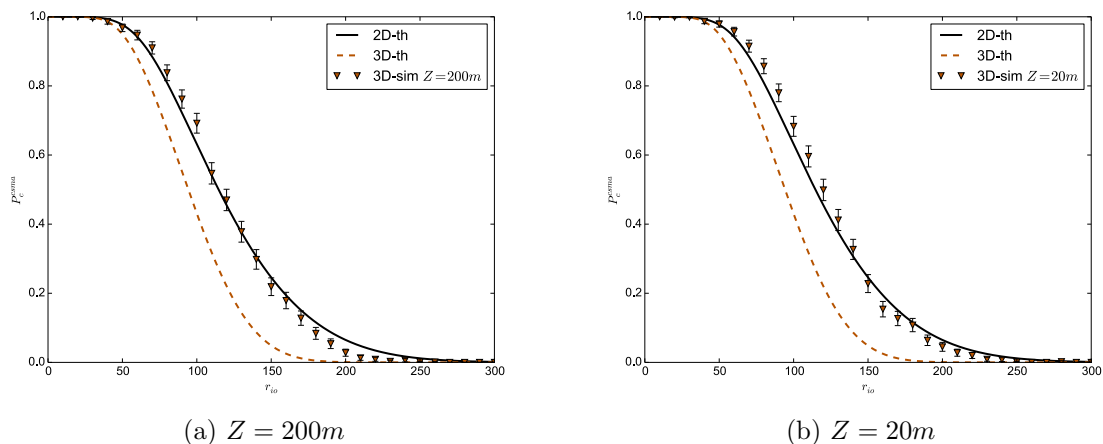


Figure 11: Comparison of theoretical and simulation results for the MMP model for  $T_d = -76\text{dBm}$

Figs. 11a and 11b present the same comparison as Fig. 10 but for more reasonable simulated  $Z$ :  $200\text{m}$  and  $20\text{m}$ . In these cases, the 3D model is in saturated condition and we observe as in Fig. 7, that the theoretical predictions of the 2D and 3D models differ. Interestingly, for both  $Z = 200\text{m}$  and  $Z = 20\text{m}$  the simulation results are closer to the 2D theoretical predictions. We note that for  $Z = 20\text{m}$  the match with the 2D model is better than for  $Z = 200\text{m}$ , notably for the tail of the curve. These results can be explained by the protection radius granted to the emitter thanks to the contention process. Indeed, with the considered parameters, the average

detection range is  $251m$ . Interferers are thus very rarely situated above or below the receiver in this context (building heights are  $Z = 200m$  and  $Z = 20m$ ) and so the vertical distances do not have a significant impact on the probability of coverage. We believe this account for the better match of the 2D model. This aspect is explicated in more details with the second simulation setup further in this section.

The second simulation setup is similar to the first except for  $T_d = -60dBm$  and  $P_t = 1mW$  (realistic for a typical WSN low power radio [24]) and the simulation box size is reduced to  $200m \times 200m \times Z$  with  $Z \in 20m, 50m, 75m, 100m, 200m$ .

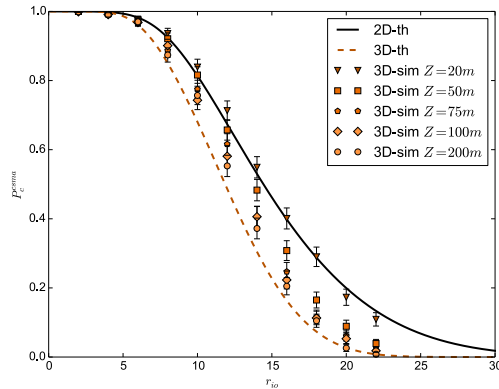


Figure 12: Comparison of theoretical and simulation results for the MMP model for  $T_d = -60dBm$

Fig. 12 shows a comparison of the simulation results with 2D and 3D models for the second simulation setup. We are, again, in saturated conditions. In this case, we observe that the simulation results are distributed between the 2D and 3D theoretical models. When  $Z$  increases the 3D model is a better match for the simulations results, while the 2D is better for smaller  $Z$ .

Intuitively this result can be understood because the CSMA detection radius (carrier sense mechanism) impede transmitter nodes to lie above one another when the building size is comparable to the size of the detection zone. If transmitters cannot be one above another, the 3D model is not able to accurately model the interference. In Fig. 13, we plot the positions of transmitters in one simulation instance with their average detection zone for

different building sizes. We observe that the transmitters are approximately on a plane for a small building height ( $Z=20\text{m}$ ), whereas they are more distributed along the  $z$  axis for larger building sizes.

In order to gain insight on this result, let us consider the probability for a node A, selected for transmission (in  $\Phi_m$ ) in the building, to have a node B, also selected for transmission, at distance  $r$ . For the coexistence of these two nodes, two cases are possible: either A has the smallest mark and B does not detect A, or B has the smallest mark and A does not detect B:

$$\begin{aligned} P(|AB| = r) &= P(P_t h_{AB} r^{-\alpha} < T_d) P(m_A < m_B) \\ &\quad + P(P_t h_{BA} r^{-\alpha} < T_d) P(m_B < m_A) \\ &= 1 - e^{-\mu T_d r^\alpha / P_t}, \end{aligned} \tag{20}$$

with  $h_{BA}$  and  $h_{AB}$  both exponentially distributed with parameter  $\mu$  and are independent, and  $P(m_A < m_B) = P(m_B < m_A) = \frac{1}{2}$ . Equation (20) is plotted in Fig. 14 with the same parameter values as the simulations in Fig. 12. We observe that it is very unlikely that two nodes selected for transmissions in CSMA can be at less than 20 meters. In fact, we can see that nodes are not likely to lie closer to each others than their average detection distance, which is 32m in this case. If the building height is 20 meters, then we cannot have one node above another node and thus the 2D model is more relevant. When the building height increases, it becomes possible to have nodes above/under others, and thus we have multiple layers of nodes (as can be observed in Figs. 13b and 13c). In order for the 3D model to become really relevant, we need to have interferers above the nodes as well as under. In order to have this, we need the building to be high enough so that the probability of having three layers of nodes is not too low. We see in Fig. 13b, that for 75m it does not happen. In fact, we would need a building height of more than 3 times the average detection radius to be confident in having 3 layers. In that case, nodes in the middle layer would experience 3D interference. Consequently, for heights from 2 to 3 times the average detection radius, the results lie between 2D and 3D models as can be seen in Fig. 12.

In this section, we highlighted the fact that in the CSMA case, the model has to be chosen carefully. Indeed, the 3D model seems to be relevant only if the average detection radius is much smaller than the building height which is not the case for 802.11. Nevertheless, this model is satisfying for low power low range communications for which the detection range is much smaller.

## 5. Conclusion and future works

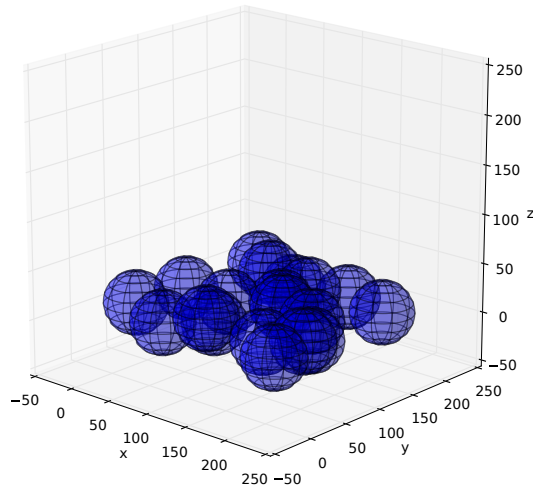
In this paper, we investigate the probability of coverage in the 3D case for two models: PPP and MMP. We show that abusively considering 2D networks when they are 3D can lead to either overestimating or underestimating the probability of coverage depending on the model parameters. We also notice interesting differences in the integral forms of the expressions when going from 2D to 3D which notably affect their tractability.

By comparing the models with simulations, we observe that the 3D model is relevant in the PPP case even if the height of the simulation box is small compared to its length and width. In the MMP case for the modeling of CSMA, it depends on the detection radius. If the detection radius is larger than the building height, the 2D model is closer to the simulations, otherwise, the 3D model is more relevant.

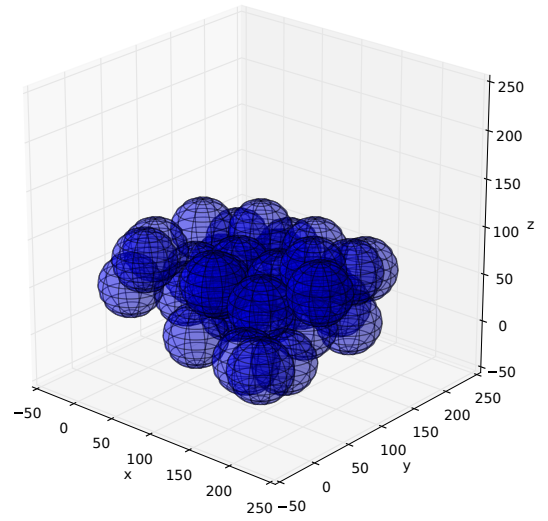
Beside the results on stochastic geometry, this work can be seen as an incentive to use 3D model and 3D simulation layouts for the design and evaluation of protocol which is seldom done in reality. Section 4.2.2 suggests that it is especially important for the design of low range IoT protocols in dense urban areas.

In the future, we plan to compare the model with traces collected in dense urban areas in order to validate our theoretical predictions and simulations. A comparison with large scale realistic simulations (notably including a more realistic propagation model) would also be useful to the community. Up to our knowledge, no study comparing high fidelity simulation or experimental results to stochastic geometry models are available.

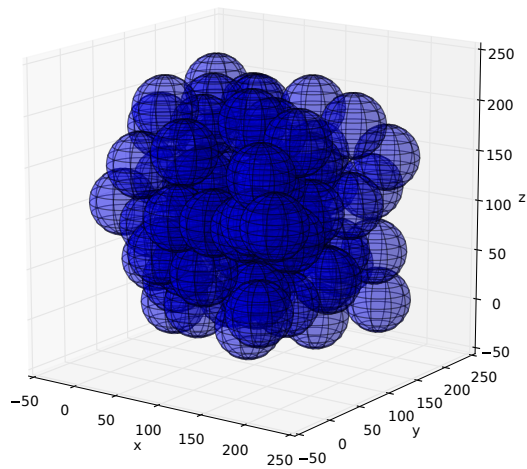
Moreover, it would be interesting to develop the 3D models by introducing a fourth dimension in the process in order to account for the packet arrivals which are spread in time.



(a)  $Z = 20m$



(b)  $Z = 75m$



(c)  $Z = 200m$

Figure 13: Instances of  $\Phi_m$  for different building heights with the average detection zone represented as a sphere ( $32m$  radius)

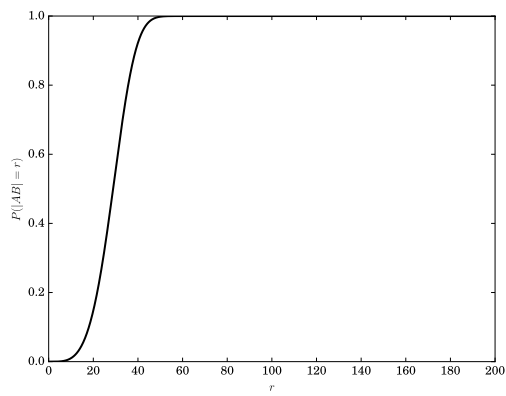


Figure 14:  $P(|AB| = r)$  with  $\mu = 1$ ,  $P_t = 1mW$ , and  $T_d = -60dBm$

## Appendix A. Derivation of equation (10)

$$\begin{aligned}
P_{csma} &= \sum_{k=0}^{+\infty} \sum_{n=k}^{+\infty} \frac{1}{1+k} P_n \binom{n}{k} P_d^k (1-P_d)^{n-k} \\
&= \sum_{k=0}^{+\infty} \sum_{n=k}^{+\infty} \frac{1}{1+k} P_n \frac{n!}{k!(n-k)!} P_d^k (1-P_d)^{n-k} \\
&= \sum_{k=0}^{+\infty} \sum_{n=k}^{+\infty} \frac{1}{(1+k)!} \frac{K^n e^{-K}}{n!} \frac{n!}{(n-k)!} P_d^k (1-P_d)^{n-k} \\
&= e^{-K} \sum_{k=0}^{+\infty} \frac{P_d^k}{(1+k)!} \sum_{n=k}^{+\infty} \frac{K^n}{(n-k)!} (1-P_d)^{n-k} \\
&\stackrel{(*)}{=} \frac{e^{-K}}{K P_d} \sum_{k=0}^{+\infty} \frac{(K P_d)^{k+1}}{(1+k)!} \sum_{m=0}^{+\infty} \frac{K^m}{(m)!} (1-P_d)^m \\
&= \frac{1 - e^{-K P_d}}{K P_d},
\end{aligned}$$

at step (\*) we let  $m = n - k$ . The differences with the 2D case [13, 14] are to be found in the expression of  $K = \rho(4/3)\pi r_d^3$  and  $P_d$  given by Equation (11).

## Appendix B. Derivation of equation (15)

$$\begin{aligned}
P_c^{csma} &= 1 - \sum_{k=1}^{+\infty} \sum_{n=k}^{+\infty} \sum_{l=1}^k P_n \binom{n}{k} (1 - P_{d'})^k P_{d'}^{n-k} \binom{k}{l} P_\beta^l (1 - P_\beta)^{k-l} \\
&= 1 - \sum_{k=1}^{+\infty} \sum_{n=k}^{+\infty} \sum_{l=1}^k \frac{K_{csma}^n e^{-K_{csma}}}{n!} \frac{n!}{k!(n-k)!} (1 - P_{d'})^k P_{d'}^{n-k} \frac{k!}{l!(k-l)!} P_\beta^l (1 - P_\beta)^{k-l} \\
&\stackrel{(*)}{=} 1 - e^{-K_{csma}} \sum_{k=1}^{+\infty} \sum_{m=0}^{+\infty} \frac{K_{csma}^{m+k}}{m!k!} (1 - P_{d'})^k P_{d'}^m \sum_{l=1}^k \frac{k!}{l!(k-l)!} P_\beta^l (1 - P_\beta)^{k-l} \\
&= 1 - e^{-K_{csma} + P_{d'}} \sum_{k=1}^{+\infty} \frac{K_{csma}^k}{k!} (1 - P_{d'})^k \sum_{l=1}^k \frac{k!}{l!(k-l)!} P_\beta^l (1 - P_\beta)^{k-l} \\
&= 1 - e^{-K_{csma} + P_{d'}} \sum_{k=1}^{+\infty} \frac{K_{csma}^k}{k!} (1 - P_{d'})^k [(P_\beta + 1 - P_\beta)^k - (1 - P_\beta)^k] \\
&= 1 - e^{-K_{csma} + P_{d'}} (e^{-K_{csma}(1-P_{d'})} - e^{-K_{csma}(1-P_{d'})(1-P_\beta)}) \\
&= e^{-K_{csma} P_\beta (1-P_{d'})},
\end{aligned}$$

at step (\*) we let  $m = n - k$ . The differences with the 2D case [14] are to be found in the expression of  $K_{csma} = \rho_{csma}(4/3)\pi r_v^3$ ,  $P_{d'}$  and  $P_\beta$  given by Equations (16) and (18).

## Appendix C. MMP: the 2D case

In this appendix we give the results which allow to plot  $P_c^{csma}$  for the 2D case in Section 4. In the 2D case:

$$P_c^{csma} = e^{-K_{csma} P_\beta (1-P_{d'})},$$

with  $K_{csma} = \lambda_{csma} \pi r_v^2$  (see [13] for the derivation of  $\lambda_{csma}$ ),  $r_v$  is given by Equation (14). For  $\alpha = 4$ ,  $P_\beta$  is given by:

$$P_\beta = \frac{r_{io}^2}{r_v^2} \beta^{1/2} \arctan \left( \frac{r_v^2}{r_{io}^2 \beta^{1/2}} \right).$$

$P_{d'}$  is as follows:

$$P_{d'} = \frac{\sqrt{\pi} \operatorname{erf} \left( (r_v^2 - 2r_{io}r_v + r_{io}^2) \sqrt{\frac{\mu T_d}{P_t}} \right)}{2r_v^2 \sqrt{\frac{\mu T_d}{P_t}}} + \int_{r_v - r_{io}}^{r_v + r_{io}} \left( \frac{r_{ij}}{r_v^2} - \frac{2 \cdot r_{ij} \cdot \operatorname{asin} \left( \frac{r_{io}^2 - r_v^2}{2r_{ij}r_{io}} + \frac{r_{ij}}{2r_{io}} \right)}{\pi r_v^2} \right) e^{-\frac{\mu r_{ij}^a T_d}{P_t}} dr_{ij},$$

$r_{io}$  is the emitter-receiver distance,  $r_{ij}$  defined as in Equation (16). As mentioned in Section 3.2.5, to the best of our knowledge, numerical integration has to be used for the second term of  $P_{d'}$  in the 2D case.

- [1] F. Baccelli, B. Blaszczyszyn, Stochastic Geometry and Wireless Networks, NOW publishers, 2009.
- [2] M. Haenggi, R. K. Ganti, Interference in large wireless networks, Now Publishers Inc, 2009.
- [3] A. Uzun, E. Neidhardt, A. Küpper, Openmobilenetwork: A platform for providing estimated semantic network topology data, International Journal of Business Data Communications and Networking (IJBDCN) 9 (4) (2013) 46–64.
- [4] A. Akella, G. Judd, S. Seshan, P. Steenkiste, Self-management in chaotic wireless deployments, Wireless Networks 13 (6) (2007) 737–755.
- [5] Logement 6e arrondissement de paris, <http://www.cartesfrance.fr/Paris/%206e%20Arrondissement-75006/logement-6e%20Arrondissement%20de%20Paris.html>, accessed: 2016-01-19.
- [6] H. Zhou, S. Xia, M. Jin, H. Wu, Localized algorithm for precise boundary detection in 3d wireless networks, in: Distributed Computing Systems (ICDCS), 2010 IEEE 30th International Conference on, IEEE, 2010, pp. 744–753.
- [7] H. M. Ammari, S. K. Das, A study of k-coverage and measures of connectivity in 3d wireless sensor networks, Computers, IEEE Transactions on 59 (2) (2010) 243–257.

- [8] M. Doddavenkatappa, M. C. Chan, A. L. Ananda, Indriya: A low-cost, 3d wireless sensor network testbed, in: *Testbeds and Research Infrastructure. Development of Networks and Communities*, Springer, 2012, pp. 302–316.
- [9] J.-H. Cui, J. Kong, M. Gerla, S. Zhou, The challenges of building mobile underwater wireless networks for aquatic applications, *Network*, IEEE 20 (3) (2006) 12–18.
- [10] J. Valente, D. Sanz, A. Barrientos, J. d. Cerro, Á. Ribeiro, C. Rossi, An air-ground wireless sensor network for crop monitoring, *Sensors* 11 (6) (2011) 6088–6108.
- [11] P. Gupta, P. Kumar, Internets in the sky: capacity of 3d wireless networks, *IEEE CDC 2000*, 2000, pp. 2290–2295.
- [12] P. Li, M. Pan, Y. Fang, The capacity of three-dimensional wireless ad hoc networks, *IEEE INFOCOM 2011*, 2011, pp. 1485–1493.
- [13] H. Q. Nguyen, F. Baccelli, D. Kofman, A stochastic geometry analysis of dense IEEE 802.11 networks, in: *IEEE INFOCOM*, 2007, pp. 1199–1207.
- [14] H. ElSawy, E. Hossain, A modified hard core point process for analysis of random csma wireless networks in general fading environments, *IEEE Transactions on Communications* 61 (4) (2013) 1520–1534.
- [15] A. Gupta, X. Zhang, J. Andrews, Sinr and throughput scaling in ultra-dense urban cellular networks, *Wireless Communications Letters*, IEEE-[doi:10.1109/LWC.2015.2472404](https://doi.org/10.1109/LWC.2015.2472404).
- [16] M. Kaynia, N. Jindal, G. E. Oien, Improving the performance of wireless ad hoc networks through MAC layer design, *IEEE Transactions on Wireless Communications* 10 (1) (2011) 240–252.
- [17] A. Hasan, J. G. Andrews, The guard zone in wireless ad hoc networks, *IEEE Transactions on Wireless Communications* 6 (3) (2007) 897–906.
- [18] D. Stoyan, W. S. Kendall, J. Mecke, L. Ruschendorf, *Stochastic geometry and its applications*, Vol. 2, Wiley New York, 1987.

- [19] A. Goldsmith, *Wireless communications*, Cambridge university press, 2005.
- [20] lorawantm specification v1.0, lora alliance, jan 2015.
- [21] Lora alliance, <https://www.lora-alliance.org/>, accessed: 2016-01-19.
- [22] E. S. Sousa, J. Silvester, et al., Optimum transmission ranges in a direct-sequence spread-spectrum multihop packet radio network, *IEEE JSAC* 8 (5) (1990) 762–771.
- [23] M. Haenggi, Mean interference in hard-core wireless networks, *IEEE Communications Letters* 15 (8) (2011) 792–794.
- [24] CC1100 Low-Power Sub- 1 GHz RF Transceiver, <http://www.ti.com/lit/ds/symlink/cc1100.pdf>, accessed: 2016-01-29.